J Mater Sci (2018) 53:13643–13659

Mechanochemical Synthesis

Mechanochemical preparation of nanocrystalline metal halide phosphors

Jun Zhang[1], Nicolas Riesen[2,3,*], Lubina Thattamveedu Kasim[1], Kate Badek[1], and Hans Riesen[1,*]

[1] School of Physical, Environmental and Mathematical Sciences, The University of New South Wales, Canberra, ACT 2600, Australia
[2] School of Engineering, University of South Australia, Mawson Lakes, Australia
[3] Institute for Photonics and Advanced Sensing (IPAS) and School of Physical Sciences, The University of Adelaide, Adelaide, Australia

Received: 27 February 2018
Accepted: 8 June 2018
Published online: 19 June 2018

ABSTRACT

In recent years, mechanochemistry has experienced a massive resurgence allowing for solvent-free preparation of many important materials with minimal energy requirements. This paper provides a review of the mechanochemical preparation of nanocrystalline metal halides for applications as inorganic phosphor materials. The review puts strong emphasis on our recent work on optical and X-ray storage phosphors such as the matlockite BaFCl:Sm^{3+}. In addition, previously unpublished results are presented including the effect on the samarium oxidation state when using ball-milling, as well as results on other rare earth-doped matlockites. We outline how mechanochemical methods can be applied to synthesise, without the need for solvents and high temperatures, a wide range of halides ranging from the most important commercial X-ray storage phosphor BaFBr:Eu^{2+} to lead perovskites of the formula $APbX_3$ with A = Cs^+, $CH_3NH_3^+$, etc., and X = F, Cl, Br, I or a mixture thereof. We also demonstrate that a wide variety of solid solutions of the general formula $M^1_xM^2_{1-x}FX^1_yX^2_{1-y}$ (with M^1 and M^2 = Ba, Sr, Ca; X^1, X^2 = Cl, Br, I) that can be suitable hosts for luminescent activator ions, can be prepared by mechanochemical methods. Importantly, for prolonged grinding times with a high-energy ball-mill, crystallites on the nanoscale can be obtained as can be confirmed by Rietveld refinements of powder XRD patterns and electron microscopy.

Introduction

Mechanochemical preparation methods are likely the oldest form of chemical synthesis, dating back thousands of years [1, 2]. Whilst the making of fire by cavemen by rubbing pieces of wood together to cause friction and then combustion is arguably a mechanochemical process, the first documented report of a mechanochemical reaction appears to be the preparation of mercury from cinnabar by

Address correspondence to E-mail: nicolas.riesen@unisa.edu.au; h.riesen@adfa.edu.au

https://doi.org/10.1007/s10853-018-2559-y

grinding [3]. In the early period of modern science, mechanochemistry however played only a minor part [4] although it did receive the attention of highly prominent nineteenth-century scientists such as Michael Faraday [5].

Mechanochemical synthesis is based on solid-state reactions that are facilitated by mechanical energy with no or minimal solvent [6]. For example, a simple kind of mechanochemistry utilises just a mortar and pestle and the solid-state reaction is induced by the grinding of the reagents, i.e. mechanochemistry achieves chemical transformations by milling or grinding without requiring bulk dissolution of reagents.

In recent years, mechanochemistry has experienced a massive resurgence not only because it allows for the solvent-free preparation of important materials but also because it reduces the energy requirements [1–5, 7]. In addition, mechanochemistry allows for the preparation of homogeneous solid solutions that are otherwise difficult to prepare since solvent-based chemistry or high-temperature synthesis often results in phase separations.

Many inorganic salts are synthesised by sintering the reagents at high temperatures, whilst quite often the same compounds can be prepared at room temperature by mechanochemical means although this is still not widely applied. Moreover, mechanochemical synthesis, in particular, high-energy ball-milling, also allows for the preparation of particles on the nanoscale [8, 9]. This is particularly important given that nanoscale materials are attracting vast attention due to their unique properties that can lead to various technological and medical applications [10–12].

As alluded to before, green chemistry has been one of the main motivators for the resurgence of mechanochemistry [7, 10, 13], since the need for multiple solvents is eliminated, often making the synthesis inherently cleaner and more efficient. As an example, the mechanochemical process is a cleaner alternative for the synthesis of pharmaceutical phenol hydrazones [14]. In many cases ball-milling can lead to higher yields with lower energy consumption even compared to alternative solvent-free reaction methods. For example, the mechanochemical-based Suzuki–Miyaura coupling of phenylboronic acid with aryl bromides showed higher yields and a significant reduction in energy usage compared to microwave irradiation-based synthesis [15]. In addition, mechanochemistry only requires simple equipment that is widely available in chemistry laboratories and it provides new possibilities for synthesising molecules and materials that would otherwise be difficult to achieve [16, 17].

In recent times mechanochemical transformations conducted by milling or grinding have emerged as versatile and powerful alternatives to conventional synthesis of organic molecules, coordination polymers and frameworks, and co-crystals. In these systems, mechanochemical reactivity was shown to provide access to noticeable reductions in the use of solvent and energy and provided enhanced control of reaction stoichiometry [18]. In addition to material synthesis, mechanochemistry can also be used to allow for the separation and recovery of chemical species and components from minerals and waste materials through another chemical and/or physical operation [19]. Significant progress has also been made towards the understanding of mechanochemistry. Urakaev et al. [20–24] have for instance made seminal contributions to delineating the mechanism and kinetics of mechanochemistry.

In the present article, we provide a review of our recent work on the mechanochemical preparation of nanocrystalline metal halides that have significant potential for applications as phosphors. For example, we have recently shown that the nanocrystalline X-ray storage phosphors BaFCl:Sm^{3+} and BaFBr:Eu^{2+} can be prepared by ball-milling [25, 26]. In addition, we provide a range of novel findings that extend upon the current literature. (Note: figure captions indicate whether results are novel or have previously been published).

Background and context

In order to provide a wider context of our work on phosphors, the following section provides a brief and non-exhaustive overview of a selection of related compounds that have been successfully synthesised mechanochemically. This includes alkali metal halides, alkaline earth metal halides and, more generally, metal halides.

There are many examples in the literature of the synthesis of alkali metal halides using mechanochemistry. Seiffert et al. for instance reported the mechanochemical preparation of AX/BX/(H_2O) with A, B = alkali metal and X = halide and the resulting solid solutions [27]. Moreover, Valor

et al. studied the interactions of potassium bromide with alkali fluorides (LiF, NaF, KF, CsF) by milling. They discovered that when grinding AX and BX (A, B = Na, K, Rb, Cs; X = Cl, Br, I) reactions only occur when the salt crystals are stable at room temperature [28]. Simple AMX_3 compounds where A is an alkali metal and M is a divalent metal and X is a halide have also been prepared successfully by milling according to the scheme in Eq. (1):

$$AX + MX_2 \rightarrow AMX_3 \quad (1)$$

For example, mechanochemical synthesis of $NaMF_3$ (M = Fe, Mn, Ni) has previously been demonstrated, with such compounds being e.g. prime candidates for positive electrode materials in sodium batteries [29]. Moreover, an early review of mechanochemical reactions in alkali halide discs was given in Ref. [30]. The mechanochemical approach has also been applied to the synthesis of carnallite-type double salts (e.g. $AMgB_3{\cdot}6H_2O$, A = K, Cs; B = Cl, Br) [31]. Furthermore, Scholz et al. demonstrated cryolite (Na_3AlF_6) and chaolite ($Na_5Al_3F_{14}$) synthesis with high-energy ball-milling [32], with the former potentially having applications within insecticides. The mechanochemical approach has also been used to synthesise ternary zinc fluorides $AZnF_3$ (A = K, Na, NH_4) [33] and complex fluorides ARF_4 (A = Li, Na, K; R = rare earth) having potential applications as solid electrolytes [34]. Similarly, Dimov et al. demonstrated the ball-milling of $NaMF_3$ (M = Mn, Fe, Co, Ni, Cu) compounds for studies into next-generation batteries [35]. Mechanochemical synthesis of the ternary halides $KMCl_3$ (M = Ti, Cr, Mn, Fe, Co, Ni, Cu, Zn) has also been reported [36].

Most demonstrations of mechanochemical synthesis utilise ball-milling with e.g. planetary ball-mills. Such techniques have been used for the fast solvent-free synthesis of many materials including basic alkaline earth metal halides. Dreger et al. however also showed that basic MF_2 (M = Mg, Ca, Sr, Ba) systems can be synthesised simply by mixing or manual shaking [37, 38]. Moreover, the preparation of nanocrystalline materials by mechanochemical approaches has been shown to improve the ionic conductivity of BaF_2, CaF_2 and SnF_2:PbF_2 mixtures [39]. Another example is given by nanocrystalline BaF_2:CaF_2 composites (10–20 nm crystallite size) prepared by high-energy ball-milling for which DC conductivities as high as 0.1 mS cm^{-1} at 450 K were reported [40]. This extraordinary conductivity was due to the diffusivity of fluorine in the composites. This initial report was followed up by more extensive investigations [41, 42]. Very recently, Wilkening et al. reported that in nanocrystalline LaF_3:SrF_2 ceramics prepared mechanochemically, the conductivity increases by several orders of magnitude [43]. Related studies on solid solutions $M^a_{1-x}M^b_xF_2$ (M = Ca, Sr, Ba), $Sr_{1-x}Y_xF_{2+x}$ ($x = 0\ldots0.5$) and MgF_2–MF_2 (M = Ca, Sr, Ba) prepared mechanochemically were also reported by Scholz and Kemnitz et al. [44–46]. Furthermore, Rongeat et al. demonstrated $Ba_{1-x}La_xF_{2+x}$ synthesis with ball-milling for potential applications as electrolytes for fluoride ion batteries [39]. The mechanochemical approach has also been used to synthesise other alkaline earth metal halides including fluorides such as $Ca_{1-x}La_xF_{2+x}$ [47]. Mechanochemical synthesis of ternary halides such as AB_2X_4 (A = Mg, Mn, Zn; B= Li, Na; X = Cl, Br) has also been reported [48].

There are many examples in the literature of other metal halides synthesised by mechanochemical means. Here we discuss a limited selection of these. Lee et al. for instance demonstrated the mechanochemical synthesis of LaOX (X = Cl, Br) as an alternative to solid-state synthesis at high temperatures [49]. Bowmaker et al. have shown that mechanochemical synthesis can be used in copper (II) halide/pyridine systems $Cu(py)_mXY$ (py = pyridine; X, Y = Cl, Br, I) [50], illustrating that this approach is applicable to redox reactions and complex syntheses with up to five components. Hernandez et al. demonstrated the mechanochemical synthesis of $M(CO)_5X$ (M = Re, Mn; X = Cl, Br, I) systems which are used as precursors of luminescent rhenium organometallics, catalysts and complexes of $[Re(CO)_3]^+$ as used for the in vitro assessment of ^{99m}Tc complexes in radiopharmaceutical and imaging applications [18]. The mechanochemical approach has also been used to synthesise other metal halides including fluorides such as $La_{1-y}Ca_yF_{3-y}$ [51] and complex metal fluoride KMF_3 (M = Mg, Zn, Mn, Ni, Cu and Co) systems [52]. In an interesting and recently published paper, the influence of reagents on the orthorhombic and cubic phase PbF_2 (e.g. lead(II) acetate, lead(II) oxide, lead(II) carbonate, NH_4F, NH_4HF_2) prepared by high-energy ball-milling was reported [53]. Also, the preparation of the cubic perovskites KMF_3 (M = Mg, Ca, Mn, Fe, Co, Ni

and Zn) by ball-milling equimolar mixtures of KF and MF_2 has been reported [54].

Materials and methods

Mechanochemical synthesis in our work was exclusively undertaken by using a high-energy ball-mill (shaker mill Retsch MM200 with a 10-mL zirconia-lined jar and two 12-mm, 5.5 g zirconia balls). Typically, a maximum total mass of ~ 0.5 g of the reagents (i.e. ball to reagent mass ratio of 21:1) was used and the mill was operated at 20 Hz. Both hydrous and anhydrous salts were used in the preparation step. As an example of a typical preparation method for a samarium-activated phosphor, a mixture of 0.2 g (1.59 mmol) SrF_2, 0.194 g (0.79 mmol) $BaCl_2{\cdot}2H_2O$, 0.237 g (0.79 mmol) $BaBr_2$ and 2.7 mg (7×10^{-3} mmol) $SmCl_3{\cdot}6H_2O$ was ball-milled for 90 min. The powder was then removed from the ball-mill jar and dried at 60 °C and then ball-milled for another 90 min to render nanocrystalline $Ba_{0.5}Sr_{0.5}FBr_{0.5}Cl_{0.5}:Sm^{3+}$.

The resulting powders were characterised by powder XRD (Rigaku MiniFlex 600), electron microscopy (SEM and TEM) and optical spectroscopy, including cathodoluminescence. For the SEM and TEM imaging, the particles were dispersed in dichloromethane or ethanol and imaged using a FEI Tecnai G2 Spirit TEM or a field emission SEM (FEI Quanta 450 FEG, 10 kV) in the secondary electron mode, respectively. Scanning electron microscopy was also conducted on a JEOL 7001 field emission scanning electron microscope.

Optical spectroscopy was conducted using a range of systems, including a Spex Horiba Jobin–Yvon Fluoromax-3, a Spex 0.5-m monochromator equipped with Andor cameras (DV401A-BV Si CCD and DU490A-1.7 InGaAs camera), a Spex 1704 1-m monochromator equipped with an Andor CCD camera and a Shimadzu UV-2450 reflectance spectrometer. For laser-based experiments, Toptica DL110 external cavity diode lasers were used around 688 nm in addition to a range of blue diode lasers around 425 nm. Appropriate interference or colour glass filters were applied to optimise the beam.

The X-irradiation was undertaken using a Sirona HELIODENT plus dental X-ray source, the Rigaku MiniFlex 600 powder XRD or a Varian Clinac linear accelerator (RPA Hospital, University of Sydney). A mercury lamp (Oriel, 6034) was used for UV radiation.

Results

Rare earth ion-doped nanocrystalline matlockites as storage phosphors

Compounds of the general formula MFX (with M = Ca, Sr, Ba and X = Cl, Br, I) crystallise in the tetragonal matlockite (PbFCl) structure with space group P4/nmm-D_{4h}. The structure comprises of alternating cation and anion layers perpendicular to the crystal *c*-axis with the peculiar feature of the chloride ions forming anionic double layers as can be represented by $(F–Ba^{2+}–Cl–Cl^{-}–Ba^{2+})_n$. For example, for BaFCl, the Ba^{2+} ions sit in sites of C_{4v} point symmetry and are ninefold coordinated with 4 F^{-} (Ba^{2+}–F^{-}: 2.058 Å) and 4 Cl^{-} ions from the adjacent planes perpendicular to the *c*-axis (Ba^{2+}–Cl^{-}: 3.107 Å) and a 5th Cl^{-} ion along the *c*-axis (from the 2nd Cl^{-} plane) just above the first Cl^{-} plane (Ba^{2+}–Cl^{-}: 3.052 Å) [55]. Such matlockites have gained considerable interest in recent years for a variety of applications [56–63].

We have for example shown that sub-micron powders of the matlockite BaFCl doped with Sm^{3+} and synthesised by co-precipitation of $BaCl_2$ with NH_4F, are efficient X-ray and UV storage phosphors [64–66]. The average crystallite size for samples prepared in this way is typically on the scale of $300 \times 200 \times 70$ nm^3. The storage mechanism is based on the trapping of electrons at the Sm^{3+} centres upon electron–hole creation by X- or γ-rays or by photoinduced electron transfer from oxide impurities in the matlockite host [67]. The resulting Sm^{2+} ions can then be readout by photoexciting the narrow $^5D_J \rightarrow {}^7F_J$ *f–f* transitions in the red region of the spectrum via the parity-allowed *f–d* transitions around 417 nm.

The behaviour of the co-precipitated BaFCl:Sm^{3+} upon exposure to 6MV LINAC radiation is illustrated in Fig. 1. It is noted here that much lower doses are required to get the same effect when irradiation is conducted in the diagnostic X-ray region (20–100 kV), where the material strongly absorbs. In addition, similar $Sm^{3+} \rightarrow Sm^{2+}$ reduction effects are observed upon exposure to UV-C light.

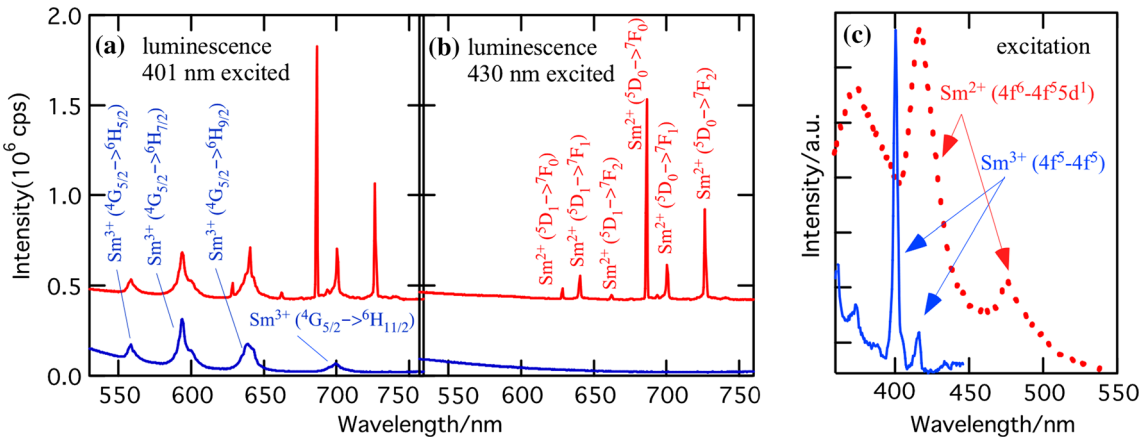

Figure 1 Luminescence and excitation spectra of co-precipitated nanocrystalline BaFCl:Sm^{3+} before (blue lower trace) and after (red upper trace) exposure to 10 Gy of 6 MV LINAC X-ray radiation. Panels **a** and **b** show the photoluminescence spectra with excitation wavelengths of 401 and 430 nm, respectively. The spectra of the irradiated samples are offset in the *y*-axis by 0.4 × 10^6 cps for clarity. Panel **c** shows normalised excitation spectra monitored at 595 nm (blue trace) and 687 nm (red trace) enabling the measurement of the selective spectra of Sm^{3+} and Sm^{2+}, respectively.

Importantly, the storage phosphor can also be prepared by mechanochemistry, in particular by ball-milling (shaker mill) of the reactants at 20 Hz for about 3 h [25]. The following reaction schemes then apply for the anhydrous and hydrated $BaCl_2$ salts, respectively:

$$BaCl_2 + BaF_2 + SmF_3(<1\%) \rightarrow 2BaFCl : Sm^{3+} \quad (2)$$

$$BaCl_2 \cdot 2H_2O + BaF_2 + SmF_3(<1\%) \rightarrow 2BaFCl : Sm^{3+} + 2H_2O \quad (3)$$

The average size of the resulting particles is on the 30-nm scale, i.e. an order of magnitude smaller than by co-precipitation. A typical TEM image of nanocrystalline BaFCl:Sm^{3+} prepared by ball-milling is given in Fig. 2.

The powder XRD diffraction patterns of BaFCl:Sm^{3+} obtained by co-precipitation and ball-milling are compared in Fig. 3. The larger widths of the diffraction peaks clearly indicate the 10 × smaller crystallites for the case of ball-milling. A crude approximation for average particle size is given by the Scherrer equation [68]:

$$D = \frac{k\lambda}{\beta \cos\theta} \quad (4)$$

where λ is the wavelength of the X-rays, k is a constant (typical value used is 0.89), and β is the full width at half maximum (FWHM) of the diffraction peak, corrected for instrumental broadening, at angle θ. A more accurate analysis of average crystallite size

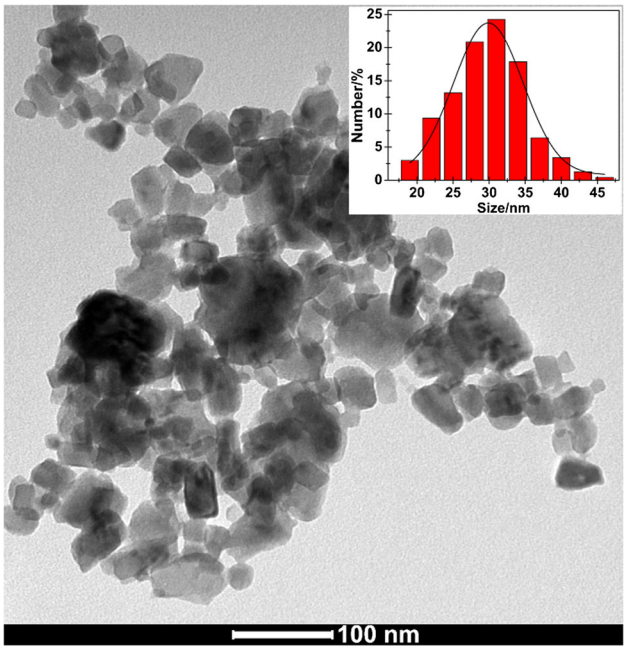

Figure 2 Representative TEM image of BaFCl:Sm^{3+} prepared by ball-milling. The inset shows a histogram that is based on a size analysis of 235 crystallites across 15 TEM images. The solid line shows a Gaussian fit to the distribution.

that takes into account strain employs the Williamson–Hall analysis [69] as given by Eq. (5),

$$\beta^2 \cos^2(\theta) = \left(\frac{\lambda}{D}\right)^2 + 16\varepsilon^2 \sin^2(\theta) \quad (5)$$

where β is the full width at half maximum of the diffraction peak (approximated with a Gaussian

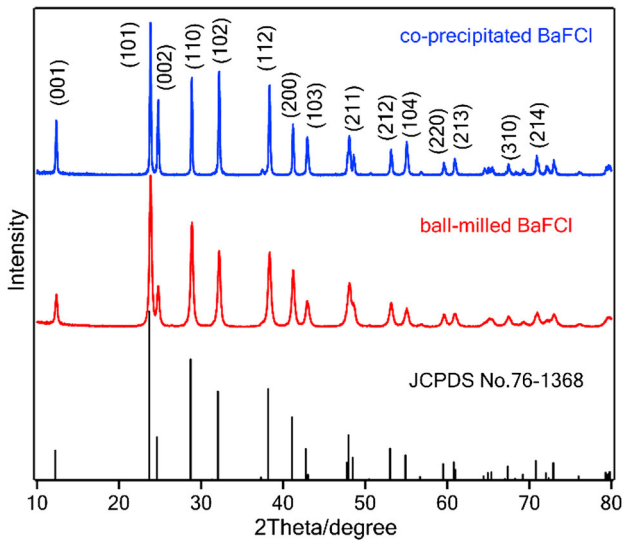

Figure 3 XRD patterns of co-precipitated and ball-milled BaFCl with the standard BaFCl powder diffraction file (JCPDS No. 76-1368).

lineshape) at angle θ corrected for the instrumental broadening, λ is the wavelength of the X-rays, and ε is a parameter describing the microstrain.

Naturally, a full Rietveld analysis (for example by Fullprof [70] or Maud [71]) of the diffraction pattern can also deliver the average crystallite size. Applying a Rietveld analysis to the powder diffraction patterns of BaFCl nanopowders prepared by ball-milling typically indicates an average crystallite size of $\sim$ 30 nm.

From a powder diffraction analysis, it appears that the presence of water molecules during crystallisation ($BaCl_2{\cdot}2H_2O$) aids the reaction and a pure matlockite phase is achieved for shorter ball-milling times [25] as is illustrated in Fig. 4.

Importantly, the kinetics of the formation of the nanocrystalline matlockite can also be followed by the evolution of the Sm^{3+} luminescence in this host as is illustrated in Fig. 5.

The sensitivity to X-ray and UV radiation of co-precipitated (250 ppm Sm^{3+}) and ball-milled BaFCl:Sm^{3+} (0.2%) is compared in Fig. 6. It follows from this experiment (Fig. 6b) that the ball-milled sample contains a significantly higher initial Sm^{2+} concentration after the preparation step. This is commensurate with the fact that relatively high local temperatures are induced by the collision of the balls in the mixer mill as is discussed in the literature [22, 72]. We have previously shown that annealing of co-precipitated samples [73] leads to a sizeable increase of the Sm^{2+} concentration with a maximum reached at 500 °C, i.e. this system could in principle serve as a temperature sensor for ball-milling processes. As indicated above, the UV sensitivity of these samples is based on the ubiquitous oxide impurities in matlockites [74, 75], which act as electron donors upon excitation into their absorption bands around 200 nm. In particular, the $Sm^{3+} \rightarrow Sm^{2+}$ reduction is highly efficient for exposures in the deep UV (UV-C) below 220 nm. This discovery is believed to potentially have significant ramifications for highly efficient optical data storage [65, 76].

In addition to the preparation of BaFCl, a vast variety of solid solutions of the general formula $M^1_xM^2_{1-x}FX^1_yX^2_{1-y}$ (with M^1 and M^2 = Ba, Sr, Ca; X^1, X^2 = Cl, Br, I) can be prepared. The MFX parent systems with M = Ba, Sr, Ca and X = Cl, Br, I, all crystallise in the PbFCl matlockite structure with space group P4/nmm [77]. As a consequence, these systems are fully miscible, allowing solid solutions.

For this article we investigated the tunability of the $^5D_0 \rightarrow {}^7F_0$ luminescence transition as a function of the $M^1_xM^2_{1-x}FX^1_yX^2_{1-y}$ composition, and also the X-ray and UV sensitivity of two systems as is illustrated in Fig. 7. The $^5D_0 \rightarrow {}^7F_0Sm^{2+}$ *f*–*f* transition can be tuned over $\sim$ 4 nm allowing engineering of inhomogeneous distributions. Interestingly, the X-ray exposed sample saturates at much higher levels. This may indicate that the number of samarium-oxide centres with an adequate separation for the electron transfer to occur upon UV exposure is limited, although the low penetration of the 188-nm UV light compared to X-rays may also be a contributing factor. Further work is needed to fully elucidate the reason for the difference in saturation behaviour. All the saturation curves can be fitted well with double exponential functions, indicating first-order dispersive kinetics.

Mechanochemistry can also be used for the direct preparation of alkaline earth fluorohalides doped with rare earth ions in the +2-oxidation state. For example, nanocrystalline BaFBr:Eu^{2+} can be directly prepared by ball-milling a mixture of BaF_2, $BaBr_2$ and $EuBr_2$ under a nitrogen atmosphere [26]. As shown in Fig. 8, the as-prepared nanocrystalline powder becomes an efficient photostimulable X-ray storage phosphor upon annealing at temperatures in the range of 400 to 900 °C. This mechanochemical method with subsequent annealing has the potential

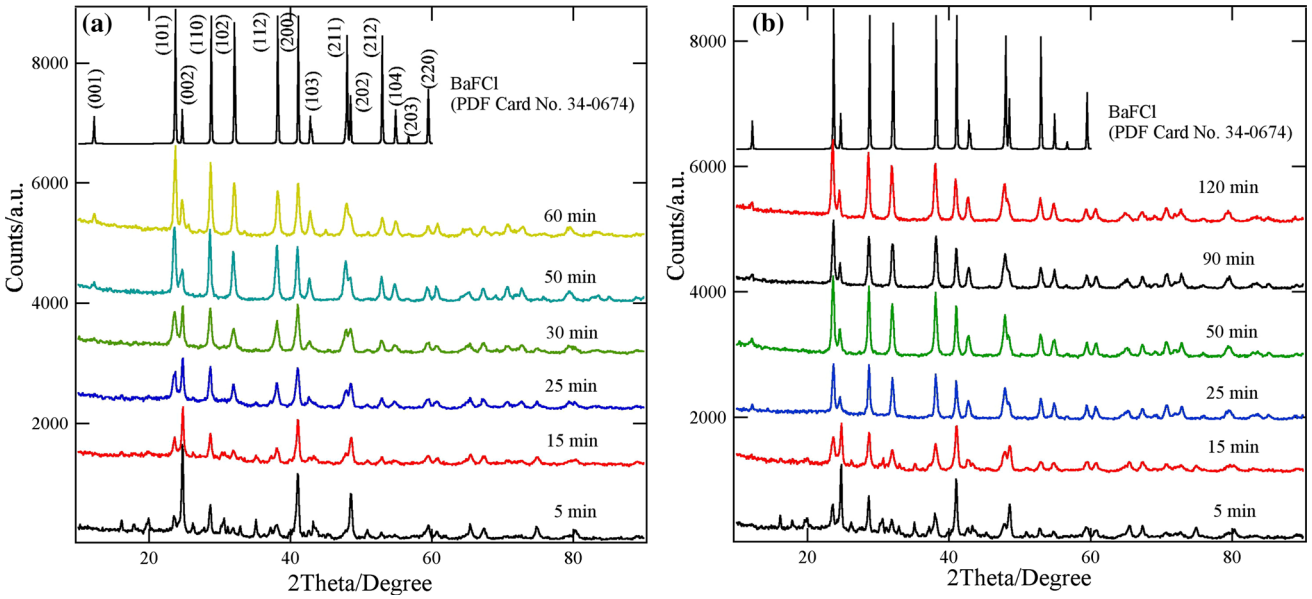

Figure 4 Powder X-ray diffraction patterns of BaFCl:Sm^{3+} as a function of ball-milling time for **a** anhydrous reagent $BaCl_2$ and **b** hydrated $BaCl_2{\cdot}2H_2O$ with BaF_2 and SmF_3. Reproduced with permission from Ref. [25], copyright 2013, Elsevier.

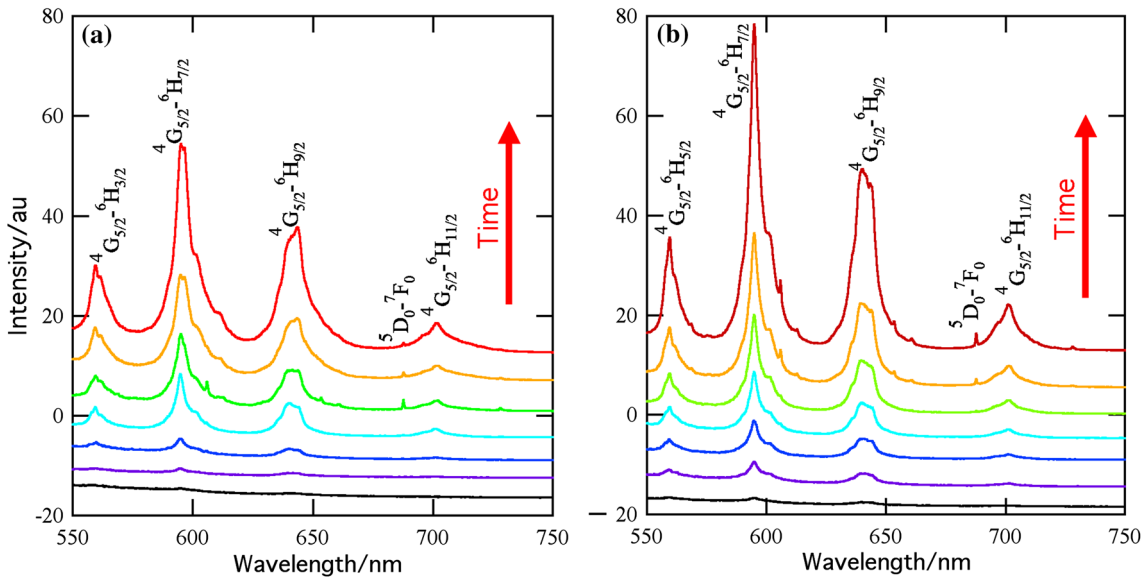

Figure 5 Evolution of the Sm^{3+} $^4G_{5/2} \rightarrow {}^6H_J$ luminescence lines with increasing periods of ball-milling (traces from bottom to top were measured after ball-milling periods of 10, 20, 30, 40, 60, 150 and 180 min) of **a** anhydrous reagent $BaCl_2$ and **b** hydrated $BaCl_2{\cdot}2H_2O$ with BaF_2 and SmF_3. Adapted with permission from Ref. [25], copyright 2013, Elsevier.

to yield photostimulable phosphors with much higher sensitivity and spatial resolution [26].

Likewise, nanocrystalline BaFCl:Sm^{2+} with different concentrations of Sm^{2+} ions can be prepared by ball-milling $BaCl_2$, BaF_2 and SmI_2 under a nitrogen atmosphere. The resulting material contains both divalent and trivalent samarium ions, but more than 90% of them were in + 2-oxidation state. This points to a significant potential for the preparation of a wide range of related X-ray and optical storage phosphors containing rare earth ions in divalent and trivalent cationic states by mechanochemical methods [78]. The successful incorporation of divalent samarium in BaFCl by ball-milling is illustrated in Fig. 9 where the

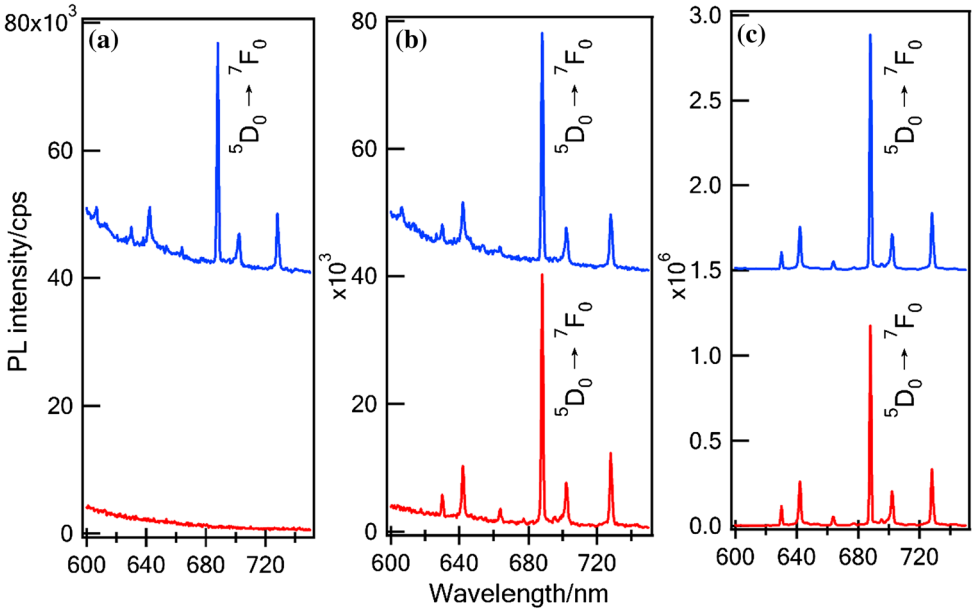

Figure 6 X-ray and UV sensitivity for co-precipitated (lower red) and ball-milled (upper blue) BaFCl:Sm^{3+}: **a** before radiation, **b** after 30-mGy X-ray (60 kV) irradiation and **c** after 20-min irradiation from a weak mercury UV light (188 nm). The $^5D_0 \rightarrow {}^7F_0$ transition of Sm^{2+} is indicated.

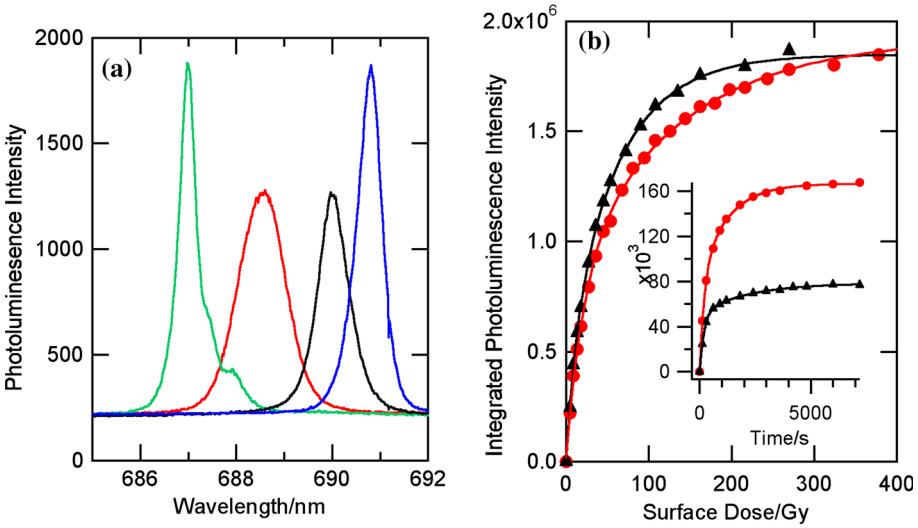

Figure 7 **a** Ball-milled $M^1_xM^2_{1-x}FX^1_yX^2_{1-y}:Sm^{3+}$ (~ 0.2%) before and after UV irradiation in the region of the Sm^{2+} $^5D_0 \rightarrow {}^7F_0$ luminescence line when excited by a 430-nm LED. From left to right: $BaFBr_{0.9}I_{0.1}$ (green), $Ba_{0.6}Sr_{0.4}FCl$ (red), $Ba_{0.1}Sr_{0.9}FCl$ (black), $Sr_{0.8}Ca_{0.2}FCl$ (blue). **b** Saturation behaviour (integrated luminescence intensity of the Sm^{2+} $^5D_0 \rightarrow {}^7F_0$ luminescence line) of $Ba_{0.6}Sr_{0.4}FCl:Sm^{3+}$ (red circles) and $Ba_{0.1}Sr_{0.9}FCl:Sm^{3+}$ (black triangles) upon X-ray and UV irradiation (the latter is given in the inset).

reflection spectrum of nanocrystalline BaFCl:Sm^{2+} prepared by ball-milling is shown.

As has been reported previously, other rare earth ions such as Yb^{3+} and Er^{3+} can also be successfully doped into alkaline earth fluorohalides by mechanochemical methods [79]. For this article we also prepared two ball-milled samples doped with Dy^{3+}, BaFCl:0.5% Dy^{3+} and SrFCl:0.5% Dy^{3+}. As is illustrated in Fig. 10, after UV radiation, divalent dysprosium Dy^{2+} occurs as can be observed by its emission lines at about 1.4 μm. These emission lines can be assigned to the $^5I_6 \rightarrow {}^5I_8$ band. The reduction upon exposure to UV light around 200 nm is again based on the photoinduced electron transfer from the

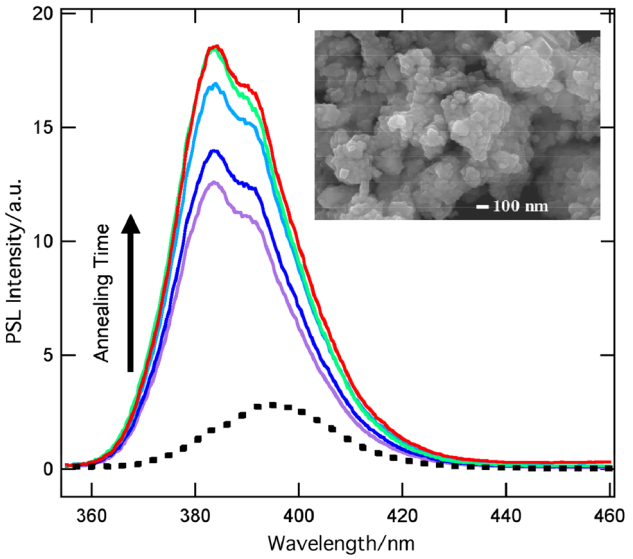

Figure 8 Intensity of the photostimulated $4f^6 5d \rightarrow 4f^7$ Eu^{2+} luminescence at 390 nm after annealing nanocrystalline BaFBr:Eu^{2+} at 900 °C for 1, 2, 3, 4, 6 h (bottom to top; 30 mGy 60 kV ESD) compared to the spectrum of a commercial imaging plate (black dotted line; 3 mGy 60 kV ESD). The luminescence was stimulated for 10 s by a red LED (634 nm; ~ 5 mW/cm^2) and the spectrum accumulated on a 0.5-m Spex spectrograph equipped with a CCD camera. The inset shows a SEM micrograph of the non-annealed sample. Adapted from Ref. [26] with permission from The Royal Society of Chemistry.

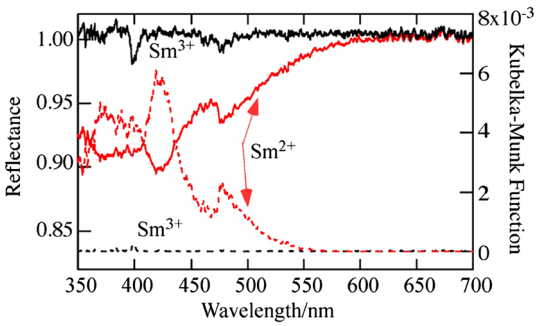

Figure 9 Comparison of the reflection spectra of nanocrystalline BaFCl:Sm^{2+} (red solid trace) and BaFCl:Sm^{3+} (black solid trace) and corresponding absorption spectra (dashed lines) as calculated by the Kubelka–Munk transformation. The intense $4f^6$-$4f^5 5d^1$ transitions around 417 nm render the BaFC:Sm^{2+} sample yellow to orange depending on the Sm^{2+} doping level. Reprinted with permission from Ref. [78]. Copyright 2014, American Chemical Society.

ubiquitous oxide impurities in matlockites, to the trivalent dysprosium. The oxide impurities have strong absorption transitions around 200 nm [65].

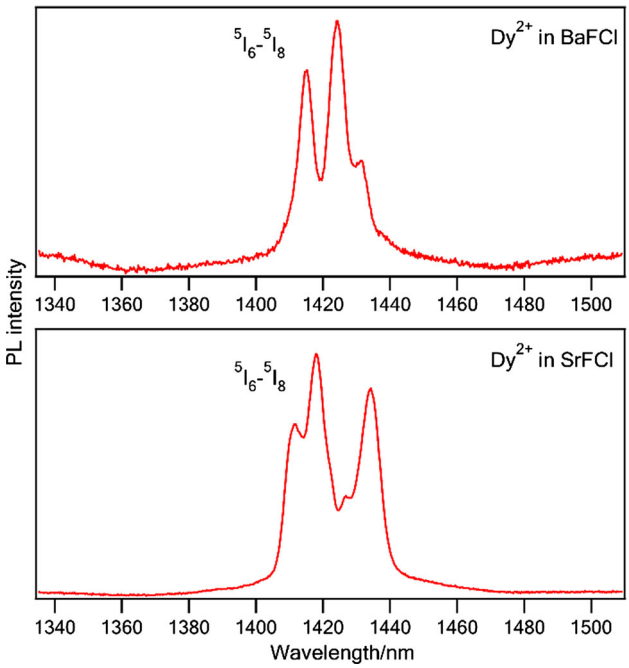

Figure 10 Photoluminescence (λ_{ex} = 462 nm) of Dy^{2+} ions in ball-milled BaFCl:0.5% Dy^{3+} and SrFCl:0.5% Dy^{3+} after UV radiation.

Samarium-doped room temperature spectral hole-burning materials

Electronic transitions in the solid state are ubiquitously broadened by variation of the local environment through lattice imperfections due to strain, unintentional impurities, point defects and isotope distributions [80]. In addition to the defects and impurities that are incorporated when using standard solvent-based crystallisation or melt-based crystal growth, mechanochemical methods may exacerbate impurity levels (material from the jar and balls) and defect densities [81]. The inhomogeneous broadening Γ_{inh} dominates at low temperature, but for many systems the homogeneous (natural) linewidth Γ_h is a significant if not dominant contribution to the width of an optical transition at room temperature since it rapidly increases with temperature due to phonon-scattering processes. In their early work, McCumber and Sturge analysed the temperature dependence of the R-lines ($^2E \leftarrow {}^4A_2$ transitions) of ruby (Al_2O_3:Cr^{3+}) above 80 K and derived the well-known ~ T^7 temperature dependence, as given by Eq. (6), for the linewidth contribution $\Delta\Gamma_{raman}$ caused by two-phonon Raman scattering of Debye phonons,

$$\Delta\Gamma_{\text{raman}} \propto \left(\frac{T}{T_D}\right)^7 \int_0^{T_D/T} \mathrm{d}x \left[x^6 \frac{\exp(x)}{(\exp(x)-1)^2}\right] \quad (6)$$

where T_D is the Debye temperature. Importantly, the T^7 dependence is a good approximation only for temperatures below 0.2 T_D.

The inhomogeneous broadening Γ_{inh} can be overcome by a range of laser techniques including spectral hole-burning [80]. This technique relies on the frequency-selective excitation of a subset of optical centres within the inhomogeneous distribution, resulting in the depletion of the ground state of the selected centres. Transient spectral hole-burning is due to population storage either in other ground-state levels or the electronically excited state. Persistent spectral hole-burning can be caused by a light-induced rearrangement of the local environment of the optical centre, leading to a shift of the transition frequency for the resonant centres, or by a photochemical process in the excited state.

In general, the luminescence properties of inorganic materials activated by samarium ions have been widely studied for their potential as solid-state lasers, luminescence materials and optical data storage media [82–84]. Much attention has been directed to Sm^{2+}-doped alkaline earth fluorohalides MFX (M = Ca, Sr, Ba; X = Cl, Br, I) ever since the first observation of photon-gated spectral hole-burning was reported for BaFCl:Sm^{2+} [85]. It is widely believed that Sm^{2+} may be the key to very high-density frequency domain optical data storage [59, 83, 86]. Importantly, Sm^{2+}-doped systems have been demonstrated to display room temperature hole-burning [59, 83, 86], a very rare phenomenon since the homogeneous linewidth usually dominates at room temperature. The *f–f* transitions are relatively immune to variations in the local environment and can also involve purely non-magnetic levels, i.e. they are not subject to electron spin flip-flops.

Mechanochemical methods enable the preparation of heavily alloyed solid solutions, allowing for an increase in the inhomogeneous linewidth. For example, $Ba_{0.5}Sr_{0.5}FBr_{0.5}Cl_{0.5}$:$Sm^{3+}$ can be readily prepared by ball-milling as is described in brief in the methods section above. As follows from the powder XRD pattern shown in Fig. 11 for a sample prepared for this article, a proper solid solution is achieved in this way with an average crystallite size of about 27 nm. Figure 11 also shows the diffraction patterns of the parent compounds with Rietveld refinements, and some of the results from these refinements are summarised in Table 1.

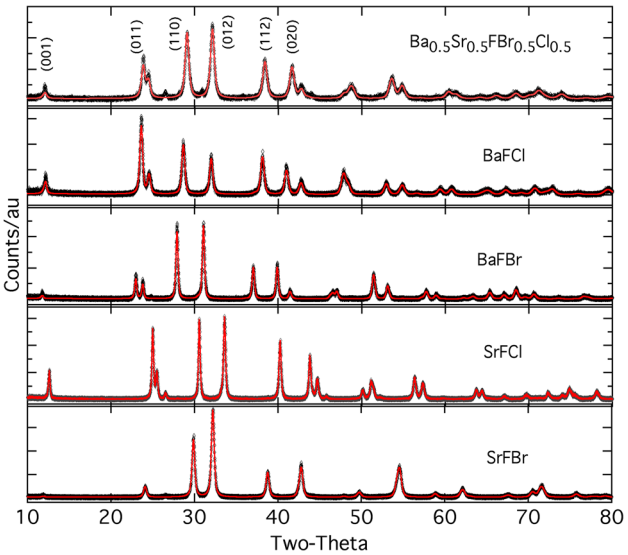

Figure 11 Diffraction pattern (black diamonds) of nanocrystalline $Ba_{0.5}Sr_{0.5}FCl_{0.5}Br_{0.5}$ and its parent compounds with Rietveld refinements (red solid lines).

Interestingly, as shown in Table 1, the unit cell lengths (a = 4.332 Å; c = 7.256 Å) of $Ba_{0.5}Sr_{0.5}FCl_{0.5}Br_{0.5}$ are approximately the average of the parent systems ($a_{average}$ = 4.317 Å; $c_{average}$ = 7.261 Å) as is expected for a proper solid solution. There appears to be a variation in crystallite size determined largely by the ball-milling time and the reagents used (anhydrous versus hydrated). The values given in Table 1 pertain to the data presented in Fig. 11. Table 1 also illustrates that there is in general a slight lattice expansion for the nanocrystallites in comparison with the bulk material in agreement with other reports [87–89].

The Sm^{3+} ion can then be switched by X-rays to the divalent oxidation state, and the latter can then be employed in spectral hole-burning experiments [90]. This is illustrated in Fig. 12 where panel (a) shows the $^5D_0 \rightarrow {}^7F_0$ luminescence line before and after X-irradiation and after spectral hole-burning. Note that the wavelength scale in Ref. [90] is incorrectly calibrated and the remeasured and fully corrected spectra are shown in Fig. 12. For comparison, the $^5D_0 \rightarrow {}^7F_0$ Sm^{2+} line is also shown for the X-irradiated BaFCl:Sm^{3+} (black dash-dot line). The observed linewidth broadens from 0.32 nm (6.7 cm^{-1}) to 1.67 nm (35 cm^{-1}) for the solid $Ba_{0.5}Sr_{0.5}FCl_{0.5}Br_{0.5}$

Table 1 Lattice parameters (P4/nmm space group) and crystallite size of nanocrystalline $Ba_{0.5}Sr_{0.5}FCl_{0.5}Br_{0.5}$ compared with MFX parent systems. For the latter, the unit cell lengths of bulk materials from Ref. [55] are given in italics within the square brackets

System	*a* (Å)	*c* (Å)	Average isotropic crystallite size (nm)
BaFCl	4.400(1) *[4.391(3)]*	7.237(2) *[7.226(4)]*	40 ± 3
BaFBr	4.516(1) *[4.503(2)]*	7.458(2) *[7.435(4)]*	64 ± 3
SrFCl	4.130(1) *[4.129(2)]*	6.976(2) *[6.966(4)]*	66 ± 3
SrFBr	4.222(1) *[4.218(2)]*	7.374(2) *[7.337(5)]*	41 ± 2
$Ba_{0.5}Sr_{0.5}FCl_{0.5}Br_{0.5}$	4.332(1)	7.256(2)	27 ± 1

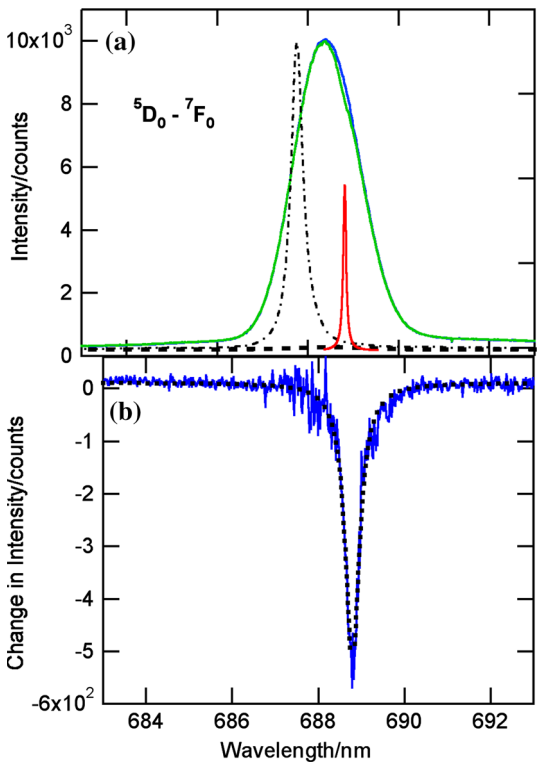

Figure 12 Spectral hole-burning in the $^5D_0$–$^7F_0$ transition of X-ray generated (9 Gy 40 kV radiation) Sm^{2+} in nanocrystalline $Ba_{0.5}Sr_{0.5}FCl_{0.5}Br_{0.5}$:$Sm^{3+}$ at room temperature. Panel **a** shows the spectrum of Sm^{2+} in the region before (dashed black trace) and after X-irradiation (solid blue trace) and after spectral hole-burning (green trace). The narrow linewidth trace shows the laser line used for the hole-burning experiment. Panel **b** shows the change in luminescence intensity upon spectral hole-burning.

solution, enabling the burning of multiple spectral holes into the inhomogeneous distribution of the $^5D_0 \rightarrow {}^7F_0$ transition. Panel (b) shows the hole-burning difference spectrum (difference of spectra before and after exposure to "resonant" laser light). The hole depth is about 5%, i.e. this is a relatively shallow hole, but much deeper holes can be burnt into this system.

Upconversion phosphors

Lanthanide-doped upconversion nanoparticles have gained considerable interest in recent years, given their capability of emitting anti-Stokes luminescence, i.e. emission at higher energy than the excitation wavelength [91–94]. Superior properties such as inertness to photo-bleaching, long-lived luminescence allowing for deep tissue penetration and relatively low toxicity, make them interesting candidates for applications ranging from 1D and 2D biosensors, to displays and photo-catalysis [95–98]. We have demonstrated that mechanochemical methods can be used to prepare efficient upconversion phosphors. For example, $NaYF_4$:Gd^{3+}/Yb^{3+}/Tm^{3+} powders prepared by ball-milling NaF, YF_3, GdF_3, YbF_3 and TmF_3 at room temperature displayed efficient

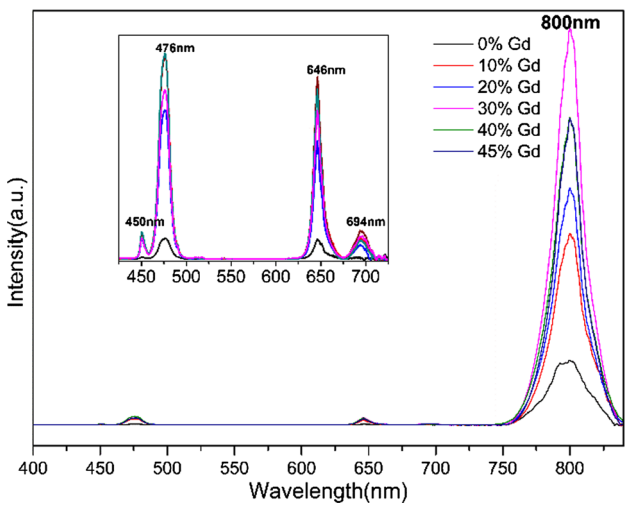

Figure 13 Upconversion luminescence spectra of $NaY_{0.89-x}Yb_{0.1}Tm_{0.01}Gd_xF_4$ (x = 0, 0.1, 0.2, 0.3, 0.4 and 0.45) samples. The inset shows the same spectra in the visible range only. Reproduced with permission from Ref. [99], copyright 2015, Elsevier B.V.

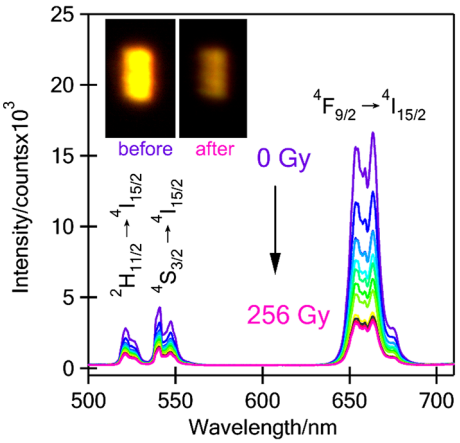

Figure 14 Upconversion luminescence spectra (excited at 980 nm) of ball-milled SrFCl:0.5% Yb^{3+}/0.1% Er^{3+} as a function of X-ray dose. Inset: corresponding photographs showing visible emissions upon 980-nm excitation (50 W cm^{-2}) before and after X-irradiation (80 Gy). Reproduced from Ref. [79] with permission from The Royal Society of Chemistry.

upconversion luminescence upon excitation by a 980-nm laser diode (see Fig. 13). XRD and TEM analyses demonstrated that the resulting materials are mainly in the hexagonal phase and are on the nanoscale with an average crystallite size of ~ 20 nm [99].

As shown in Fig. 14, ball-milled SrFCl:Yb^{3+}/Er^{3+} nanocrystals also displayed relatively efficient upconversion luminescence under 980-nm infrared excitation. Upon X-ray exposure, the upconversion luminescence intensity decreased due to the reduction of Yb^{3+} and Er^{3+} ions into their divalent state. This phenomenon can be used as a novel method for detecting ionising radiation by monitoring changes in the upconversion luminescence intensity [79].

Lead halide perovskites

Lead halide perovskites of the general formula $APbX_3$ with X = Cl, Br, I or mixtures thereof and A = $CH_3NH_3^+$, $[HC(NH_2)_2]^+$ or Cs^+ have received unprecedented attention in the history of materials science over recent years [100–103]. This frenzy of activity revolves around the fact that thin films of $CH_3NH_3PbI_3$ as the active material provide highly efficient solar energy conversion with efficiencies of up to 21%. In addition, caesium salts have a significant potential as phosphor materials for LEDs. There is no doubt that these materials display highly interesting phenomena and that they may lead to new materials that can be used effectively as low-temperature solvent-processed solar cell materials, but so far such applications still face major engineering challenges in terms of stability, e.g. moisture sensitivity, reactivity and environmental concerns.

Recently, it has been demonstrated that $CH_3NH_3PbI_3$ can be prepared without solvents via the ball-milling route [104]. A clean perovskite phase was obtained using the advantageous mechanochemical preparation method.

Figure 15 shows the powder XRD, reflectance and photoluminescence spectra of a $CsPbBr_3$ sample that was prepared for this article by ball-milling CsBr and $PbBr_2$ at 20 Hz for 90 min. The average crystallite size as determined by the Rietveld refinement was found to be 130 nm. The photoluminescence was measured on a very thin film of the material on a glass substrate, and the reflectance was measured by diluting the material into a $BaSO_4$ matrix. This figure demonstrates that the lead (or tin) perovskites can be synthesised by facile and solvent-free mechanochemical means. Importantly, the mechanochemical method

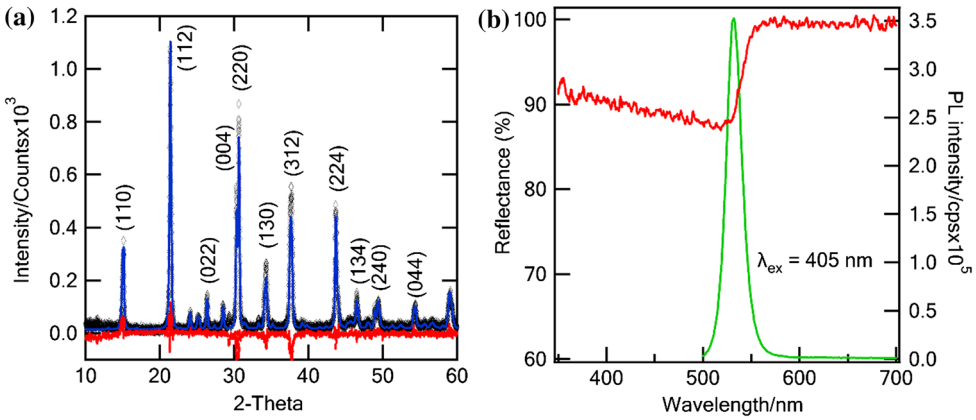

Figure 15 **a** Powder XRD pattern (black diamonds) of $CsPbBr_3$ powder with a Rietveld refinement (blue solid line). The residual is shown in red. **b** Reflectance (3 weight% $CsPbBr_3$ in $BaSO_4$) and photoluminescence (PL) spectra of the solid $CsPbBr_3$ powder.

allows for the preparation of systems that would otherwise be impossible using solvent methods, such as $CsPbCl_{3-x}I_x$.

Conclusions

Mechanochemistry offers an exciting alternative to solvent and high-temperature-based preparation methods for alkali, alkaline earth and metal halides that have potential for a wide range of optical and electro-optical applications and in particular for storage phosphors. As shown in this article, $BaFBr:Eu^{2+}$, which is the most important storage phosphor in computed radiography, can for example be prepared at room temperature by a facile ball-milling process. In many cases, it is also possible to obtain the material at the scale of tens of nanometres and for prolonged ball-milling times relatively narrow particle size distributions can be achieved. Mechanochemistry has a significant potential in the preparation of optical phosphor materials whether it be X-ray storage phosphors, UV–Vis light storage phosphors or light converters in coatings of LEDs. It is often possible to obtain pure phases (at least at the XRD level) that are otherwise difficult to achieve. It is also possible to obtain true solid solutions of rather complicated mixtures of halides which can be used in the design of optical storage materials. For example, the alloying of halides allows engineering of the inhomogeneous linewidth in order to enable room temperature spectral hole-burning that in turn could be used in frequency domain optical data storage amongst other applications.

Acknowledgements

JZ and LTK acknowledge UNSW for PhD scholarships. NR was supported by an Australian Research Council Laureate Fellowship awarded to T. M. Monro (FL130100044).

Compliance with ethical standards

Conflict of interest The authors declare that there are no conflicts of interest.

References

[1] James SL, Adams CJ, Bolm C et al (2012) Mechanochemistry: opportunities for new and cleaner synthesis. Chem Soc Rev 41:413–447

[2] Boldyrev VV, Tkáčová K (2000) Mechanochemistry of solids: past, present, and prospects. J Mater Synth Process 8:121–132

[3] Takacs L (2000) Quicksilver from cinnabar: the first documented mechanochemical reaction? JOM 52:12–13

[4] Baláž P (2000) Mechanochemistry and mechanical activation of solids. In: Baláž P (ed) Extractive metallurgy of activated minerals. Elsevier, Amsterdam, pp 1–14

[5] Harris KDM (2013) How grinding evolves. Nat. Chem. 5:12–14

[6] Gold Book (2014) Compendium of chemical terminology. In: International union of pure and applied chemistry, Version 2.3.3. pp 903

[7] Avvakumov EG, Senna M, Kosova NV (2001) Soft mechanochemical synthesis: a basis for new chemical technologies. Springer Science & Business Media, Berlin

[8] Urakaev FK, Bulavchenko AI, Uralbekov BM et al (2016) Mechanochemical synthesis of colloidal sulfur particles in the $Na_2S_2O_3$–$H_2(C_4H_4O_4)$–Na_2SO_3 system. Colloid J 78:210–219

[9] Sopicka-Lizer M (2010) High-energy ball milling: mechanochemical processing of nanopowders. Elsevier, New York

[10] Bruce PG, Scrosati B, Tarascon J-M (2008) Nanomaterials for rechargeable lithium batteries. Angew Chem Int Ed 47:2930–2946

[11] Smith BR, Gambhir SS (2017) Nanomaterials for in vivo imaging. Chem Rev 117:901–986

[12] Idris NM, Jayakumar MKG, Bansal A, Zhang Y (2015) Upconversion nanoparticles as versatile light nanotransducers for photoactivation applications. Chem Soc Rev 44:1449–1478

[13] Baig RBN, Varma RS (2012) Alternative energy input: mechanochemical, microwave and ultrasound-assisted organic synthesis. Chem Soc Rev 41:1559–1584

[14] Oliveira PFM, Baron M, Chamayou A, Andre-Barres C, Guidetti B, Baltas M (2014) Solvent-free mechanochemical route for green synthesis of pharmaceutically attractive phenol-hydrazones. RSC Adv 4:56736–56742

[15] Schneider F, Szuppa T, Stolle A, Ondruschka B, Hopf H (2009) Energetic assessment of the Suzuki–Miyaura reaction: a curtate life cycle assessment as an easily understandable and applicable tool for reaction optimization. Green Chem 11:1894–1899

[16] Katsenis AD, Puškarić A, Štrukil V et al (2015) In situ X-ray diffraction monitoring of a mechanochemical reaction reveals a unique topology metal-organic framework. Nat Commun 6:6662

[17] Wang G-W, Komatsu K, Murata Y, Shiro M (1997) Synthesis and X-ray structure of dumb-bell-shaped C_{120}. Nature 387:583

[18] Hernandez JG, Butler IS, Friscic T (2014) Multi-step and multi-component organometallic synthesis in one pot using orthogonal mechanochemical reactions. Chem Sci 5:3576–3582

[19] Zhang Q, Saito F (2012) A review on mechanochemical syntheses of functional materials. Adv Powder Technol 23:523–531

[20] Bowden FP, Persson PA (1961) Deformation, heating and melting of solids in high-speed friction. Proc R Soc Lond A 260:433–458

[21] Urakaev FK, Boldyrev V (2000) Mechanism and kinetics of mechanochemical processes in comminuting devices: 1. Theory. Powder Technol 107:93–107

[22] Urakaev FK (2013) Simulation of the mechanically induced self-propagating reactions: heat source of "viscous flow" and mechanism of MSR in Zn–S system. Combust Sci Technol 185:1281–1294

[23] Urakaev FK, Boldyrev V (2000) Mechanism and kinetics of mechanochemical processes in comminuting devices: 2. Applications of the theory. Experiment. Powder Technol 107:197–206

[24] Urakaev FK (2010) Mechanism and kinetics of mechanochemical processes. In: High-energy ball milling. Elsevier, pp 9–44

[25] Liu Z, Stevens-Kalceff MA, Wang X, Riesen H (2013) Mechanochemical synthesis of nanocrystalline BaFCl:Sm^{3+} storage phosphor by ball milling. Chem Phys Lett 588:193–197

[26] Wang X, Riesen H (2015) Mechanochemical synthesis of an efficient nanocrystalline BaFBr:Eu^{2+} X-ray storage phosphor. RSC Adv 5:85506–85510

[27] Severin I, Seifert H-J, Yariv S (1990) Mechanochemical reactions of alkali metal-halides—the systems AX/BX/(H_2O) with A, B = Na, K, Rb, Cs and X = Cl, Br, I. J. Solid State Chem 88:401–405

[28] Valor A, Fernández-Bertrán J, Radilla J (2001) On the interactions of potassium bromide with alkali fluorides. J Fluorine Chem 107:137–139

[29] Gocheva ID, Nishijima M, Doi T, Okada S, Yamaki J-I, Nishida T (2009) Mechanochemical synthesis of $NaMF_3$ (M = Fe, Mn, Ni) and their electrochemical properties as positive electrode materials for sodium batteries. J Power Sour 187:247–252

[30] Fernández-Bertrán J, Reguera E (1996) Mechanochemical reactions in alkali halide pressed disks. Solid State Ion 93:139–146

[31] Shoval S, Yariv S (1998) Formation of carnallite type double salts by grinding mixtures of magnesium and alkali halides with the same anions. J Therm Anal Calorim 51:251–263

[32] Scholz G, Korup O (2006) High-energy ball milling-a possible synthesis route for cryolite and chiolite. Solid State Sci 8:678–684

[33] Lee J, Zhang Q, Saito F (2001) Mechanochemical synthesis of ternary fluorides with perovskite structures. Chem Lett 30:700–701

[34] Lu J, Zhang Q, Saito F (2002) Mechanochemical synthesis of nano-sized complex fluorides from pair of different constituent fluoride compounds. Chem Lett 31:1176–1177

[35] Dimov N, Nishimura A, Chihara K, Kitajou A, Gocheva ID, Okada S (2013) Transition metal $NaMF_3$ compounds as model systems for studying the feasibility of ternary Li-M-F and Na-M-F single phases as cathodes for lithium–ion and sodium–ion batteries. Electrochim Acta 110:214–220

[36] Pawelke RH, Felderhoff M, Weidenthaler C, Bogdanovíc B, Schüth F (2009) Mechanochemical synthesis of ternary potassium transition metal chlorides. Z Anorg Allg Chem 635:265–270

[37] Scholz G, Meyer K, Düvel A, Heitjans P, Kemnitz E (2013) Fast ion conducting nanocrystalline alkaline earth fluorides simply prepared by mixing or manual shaking. Z Anorg Allg Chem 639:960–966

[38] Dreger M, Scholz G, Kemnitz E (2012) An easy access to nanocrystalline alkaline earth metal fluorides—just by shaking. Solid State Sci 14:528–534

[39] Rongeat C, Reddy MA, Witter R, Fichtner M (2013) Nanostructured fluorite-type fluorides as electrolytes for fluoride ion batteries. J Phys Chem C 117:4943–4950

[40] Ruprecht B, Wilkening M, Steuernagel S, Heitjans P (2008) Anion diffusivity in highly conductive nanocrystalline BaF_2:CaF_2 composites prepared by high-energy ball milling. J Mater Chem 18:5412–5416

[41] Ruprecht B, Wilkening M, Feldhoff A, Steuernagel S, Heitjans P (2009) High anion conductivity in a ternary non-equilibrium phase of BaF_2 and CaF_2 with mixed cations. Phys Chem Chem Phys 11:3071–3081

[42] Düvel A, Ruprecht B, Heitjans P, Wilkening M (2011) Mixed alkaline-earth effect in the metastable anion conductor $Ba_{1-x}Ca_xF_2$ ($0 \leq x \leq 1$): correlating long-range ion transport with local structures revealed by ultrafast ^{19}F MAS NMR. J Phys Chem C 115:23784–23789

[43] Breuer S, Lunghammer S, Kiesl A, Wilkening M (2018) F anion dynamics in cation-mixed nanocrystalline LaF_3:

SrF_2. J Mater Sci. https://doi.org/10.1007/s10853-018-2361-x

[44] Heise M, Scholz G, Düvel A, Heitjans P, Kemnitz E (2016) Mechanochemical synthesis, structure, and properties of solid solutions of alkaline earth metal fluorides: $Ma_{1-x}Mb_xF_2$ (M: Ca, Sr, Ba). Solid State Sci 60:65–74

[45] Ritter B, Krahl T, Scholz G, Kemnitz E (2016) Local structures of solid solutions $Sr_{1-x}Y_xF_{2+x}$ (x = 0…0.5) with fluorite structure prepared by sol–gel and mechanochemical syntheses. J Phys Chem C 120:8992–8999

[46] Scholz G, Breitfeld S, Krahl T, Düvel A, Heitjans P, Kemnitz E (2015) Mechanochemical synthesis of MgF_2–MF_2 composite systems (M = Ca, Sr, Ba). Solid State Sci 50:32–41

[47] Sobolev BP, Sviridov IA, Fadeeva VI et al (2005) Mechanochemical synthesis of nonstoichiometric fluorite $Ca_{1-x}La_xF_{2+x}$ nanocrystals from CaF_2 and LaF_3 single crystals. Crystallogr Rep 50:478–485

[48] Solinas I, Lutz HD (1995) Nonceramic Preparation techniques for ternary halides AB_2X_4 with A = Mg, Mn, Zn; B = Li, Na; X = Cl, Br. J Solid State Chem 117:34–38

[49] Lee J, Zhang Q, Saito F (2001) Mechanochemical synthesis of LaOX (X = Cl, Br) and their solid state solutions. J Solid State Chem 160:469–473

[50] Bowmaker GA, Di Nicola C, Pettinari C, Skelton BW, Somers N, White AH (2011) Mechanochemical synthesis in copper(ii) halide/pyridine systems: single crystal X-ray diffraction and IR spectroscopic studies. Dalton Trans 40:5102–5115

[51] Sobolev BP, Sviridov IA, Fadeeva VI et al (2008) Mechanochemical synthesis of nonstoichiometric nanocrystals $La_{1-y}Ca_yF_{3-y}$ with a tysonite structure and nanoceramic materials from CaF_2 and LaF_3 crystals. Crystallogr Rep 53:868

[52] Manivannan V, Parhi P, Kramer JW (2008) Metathesis synthesis and characterization of complex metal fluoride, KMF_3 (M = Mg, Zn, Mn, Ni, Cu and Co) using mechanochemical activation. Bull Mater Sci 31:987–993

[53] Heise M, Scholz G, Kemnitz E (2017) Mechanochemical synthesis of PbF_2 by high energy ball milling. Solid State Sci 72:41–46

[54] Lee J, Shin H, Lee J, Chung H, Zhang Q, Saito F (2003) Mechanochemical syntheses of perovskite $KM^{II}F_3$ with cubic structure (M^{II} = Mg, Ca, Mn, Fe Co, Ni, and Zn). Mater Trans 44:1457–1460

[55] Beck H (1976) A study on mixed halide compounds MFX (M = Ca, Sr, Eu, Ba; X = Cl, Br, I). J Solid State Chem 17:275–282

[56] Hagemann H, D'Anna V, Lawson Daku M, Kubel F (2012) Crystal chemistry in the barium fluoride chloride system. Cryst Growth Des 12:1124–1131

[57] Pal P, Penhouët T, D'Anna V, Hagemann H (2013) Effect of pressure on the free ion and crystal field parameters of Sm^{2+} in BaFBr and SrFBr hosts. J Lumin 134:678–685

[58] Falin M, Bill H, Lovy D (2004) EPR of Sm^{3+} in BaFCl single crystals. J Phys: Condens Matter 16:1293

[59] Jaaniso R, Bill H (1991) Room temperature persistent spectral hole burning in Sm-doped $SrFCl_{1/2}Br_{1/2}$ mixed crystals. EPL 16:569

[60] Pal P, Hagemann H, Bill H, Zhang J (2015) Temperature and host dependence of the transition interference between f–f and f–d transitions of Sm^{2+} in matlockites. J Lumin 161:323–329

[61] Monnier A, Schnieper M, Jaaniso R, Bill H (1997) Samarium-doped thin films of the matlockite structure: design, luminescence, and hole-burning experiments. J Appl Phys 82:536–547

[62] haj Hassan FE, Akbarzadeh H, Hashemifar SJ, Mokhtari A (2004) Structural and electronic properties of matlockite MFX (M = Sr, Ba, Pb; X = Cl, Br, I) compounds. J Phys Chem Solids 65:1871–1878

[63] Mittal R, Chaplot SL, Sen A, Achary SN, Tyagi AK (2003) Lattice dynamics and inelastic neutron scattering studies of MFX (M = Ba, Sr, Pb; X = Cl, Br, I). Phys Rev B 67:134303

[64] Riesen H, Kaczmarek WA (2007) Efficient X-ray generation of Sm^{2+} in nanocrystalline BaFCl/Sm^{3+}: a photoluminescent X-ray storage phosphor. Inorg Chem 46:7235–7237

[65] Riesen H, Badek K, Monro TM, Riesen N (2016) Highly efficient valence state switching of samarium in BaFCl: Sm nanocrystals in the deep UV for multilevel optical data storage. Opt Mater Express 6:3097–3108

[66] Liu Z, Stevens-Kalceff M, Riesen H (2012) Photoluminescence and cathodoluminescence properties of nanocrystalline BaFCl:Sm^{3+} X-ray storage phosphor. J Phys Chem C 116:8322–8331

[67] Riesen N, François A, Badek K, Monro TM, Riesen H (2015) Photoreduction of Sm^{3+} in nanocrystalline BaFCl. J Phys Chem A 119:6252–6256

[68] Scherrer P (1918) Estimation of the size and internal structure of colloidal particles by means of Röntgen. Nachr. Ges. Wiss. Göttingen 2:96–100

[69] Williamson GK, Hall WH (1953) X-ray line broadening from filed aluminium and wolfram. Acta Metall 1:22–31

[70] https://www.ill.eu/sites/fullprof/. Accessed February 2018

[71] http://maud.radiographema.eu/. Accessed February 2018

[72] Urakaev FK (2013) Simulation of mechanically induced self-propagating reactions: density of the heat source due to the enthalpy of reaction. Combust Sci Technol 185:723–734

[73] Liu Z, Stevens-Kalceff MA, Riesen H (2013) Effects of postannealing on the photoluminescence properties of coprecipitated nanocrystalline BaFCl:Sm^{3+}. J Phys Chem A 117:1930–1934

[74] Radzhabov E, Otroshok V (1995) Optical spectra of oxygen defects in BaFCl and BaFBr crystals. J Phys Chem Solids 56:1–7

[75] Eachus RS, Nuttall RHD, Olm MT, McDugle WG, Koschnick FK, Hangleiter T, Spaeth JM (1995) Oxygen defects in BaFBr and BaFCl. Phys Rev B 52:3941–3950

[76] Riesen N, Pan X, Badek K et al (2018) Towards rewritable multilevel optical data storage in single nanocrystals. Opt Express 26:12266–12276

[77] Kalpana G, Palanivel B, Shameem Banu IB, Rajagopalan M (1997) Structural and electronic properties of alkaline-earth fluorohalides under pressure. Phys Rev B 56:3532–3535

[78] Wang XL, Liu ZQ, Stevens-Kalceff MA, Riesen H (2014) Mechanochemical preparation of nanocrystalline BaFCl doped with samarium in the 2+ oxidation state. Inorg Chem 53:8839–8841

[79] Zhang J, Riesen N, Riesen H (2017) Mechanochemically prepared SrFCl nanophosphor co-doped with Yb^{3+} and Er^{3+} for detecting ionizing radiation by upconversion luminescence. Nanoscale 9:15958–15966

[80] Riesen H (2006) Hole-burning spectroscopy of coordination compounds. Coord Chem Rev 250:1737–1754

[81] Urakaev FK (2016) Preparation of $NaIn(WO_4)_2$ nanocrystals and a charge for crystal growth via the free-of-rubbing mechanical activation of the $Na_2CO_3 - In_2O_3 - WO_3$ system. Mendeleev Commun 26:546–548

[82] Fujita K, Yasumoto C, Hirao K (2002) Photochemical reactions of samarium ions in sodium borate glasses irradiated with near-infrared femtosecond laser pulses. J Lumin 98:317–323

[83] Mikhail P, Hulliger J, Schnieper M, Bill H (2000) SrB_4O_7:Sm^{2+}: crystal chemistry, Czochralski growth and optical hole burning. J Mater Chem 10:987–991

[84] Zeng Q, Kilah N, Riley M, Riesen H (2003) Luminescence properties of Sm^{2+}-activated barium chloroborates. J Lumin 104:65–76

[85] Winnacker A, Shelby RM, Macfarlane RM (1985) Photon-gated hole burning: a new mechanism using two-step photoionization. Opt Lett 10:350–352

[86] Cho D-H, Hirao K, Fujita K, Soga N (1996) Photochemical hole burning and local structural change in Sm^{2+}-doped borate glasses. J Am Ceram Soc 79:327–332

[87] Qin W, Chen ZH, Huang PY, Zhuang YH (1999) Crystal lattice expansion of nanocrystalline materials. J Alloys Compd 292:230–232

[88] Fukuhara M (2003) Lattice expansion of nanoscale compound particles. Phys Lett A 313:427–430

[89] Manuel DP, Péter Á, Karsten A (2012) Size-dependent lattice expansion in nanoparticles: reality or anomaly? ChemPhysChem 13:2443–2454

[90] Liu Z, Massil T, Riesen H (2010) Spectral hole-burning properties of Sm^{2+} ions generated by X-rays in BaFCl:Sm^{3+} nanocrystals. Phys Proced 3:1539–1545

[91] Haase M, Schafer H (2011) Upconverting nanoparticles. Angew Chem Int Ed 50:5808–5829

[92] Han S, Deng R, Xie X, Liu X (2014) Enhancing luminescence in lanthanide-doped upconversion nanoparticles. Angew Chem Int Ed 53:11702–11715

[93] Zhou J, Liu Q, Feng W, Sun Y, Li F (2015) Upconversion luminescent materials: advances and applications. Chem Rev 115:395–465

[94] Wang Z, Li Y, Jiang Q, Zeng H, Ci Z, Sun L (2014) Pure near-infrared to near-infrared upconversion of multifunctional Tm^{3+} and Yb^{3+} co-doped $NaGd(WO_4)_2$ nanoparticles. J Mater Chem C 2:4495–4501

[95] Carlos LD, Ferreira RAS, de Zea Bermudez V, Julian-Lopez B, Escribano P (2011) Progress on lanthanide-based organic-inorganic hybrid phosphors. Chem Soc Rev 40:536–549

[96] Liu Y, Tu D, Zhu H, Ma E, Chen X (2013) Lanthanide-doped luminescent nano-bioprobes: from fundamentals to biodetection. Nanoscale 5:1369–1384

[97] Zheng K, Liu Z, Lv C, Qin W (2013) Temperature sensor based on the UV upconversion luminescence of Gd^{3+} in Yb^{3+}-Tm^{3+}-Gd^{3+} codoped $NaLuF_4$ microcrystals. J Mater Chem C 1:5502–5507

[98] Liu Q, Feng W, Li F (2014) Water-soluble lanthanide upconversion nanophosphors: synthesis and bioimaging applications in vivo. Coord Chem Rev 273–274:100–110

[99] Zhang J, Riesen H (2015) Mechanochemical preparation of nanocrystalline $NaYF_4$:Gd^{3+}/Yb^{3+}/Tm^{3+}: an efficient upconversion phosphor. Chem Phys Lett 641:1–4

[100] Yang S, Fu W, Zhang Z, Chen H, Li C-Z (2017) Recent advances in perovskite solar cells: efficiency, stability and lead-free perovskite. J Mater Chem A 5:11462–11482

[101] Park N-G (2015) Perovskite solar cells: an emerging photovoltaic technology. Mater Today 18:65–72

[102] Protesescu L, Yakunin S, Bodnarchuk MI et al (2015) Nanocrystals of cesium lead halide perovskites ($CsPbX_3$, X = Cl, Br, and I): novel optoelectronic materials showing bright emission with wide color gamut. Nano Lett 15:3692–3696

[103] Akkerman QA, D'Innocenzo V, Accornero S, Scarpellini A, Petrozza A, Prato M, Manna L (2015) Tuning the optical properties of cesium lead halide perovskite nanocrystals by anion exchange reactions. J Am Chem Soc 137:10276–10281

[104] Elseman AM, Rashad MM, Hassan AM (2016) Easily attainable, efficient solar cell with mass yield of nanorod single-crystalline organo-metal halide perovskite based on a ball milling technique. ACS Sustain Chem Eng 4:4875–4886